

SN Ia-Cosmology Analysis Results from Simulated LSST Images: from Difference Imaging to Constraints on Dark Energy

B. Sánchez¹, R. Kessler^{2,3}, D. Scolnic¹, B. Armstrong⁴, R. Biswas⁵, J. Bogart⁶, J. Chiang^{6,7}, J. Cohen-Tanugi^{8,10},
D. Fouchez⁹, Ph. Gris¹⁰, K. Heitmann¹¹, R. Hložek¹², S. Jha¹³, H. Kelly^{6,7}, S. Liu^{14,15}, G. Narayan^{16,17}, B. Racine⁹,
E. Rykoff⁶, M. Sullivan¹⁸, C. Walter¹, M. Wood-Vasey^{14,15}

The LSST Dark Energy Science Collaboration (DESC)

¹ Department of Physics, Duke University, Durham, NC 27708, USA

² Department of Astronomy and Astrophysics, University of Chicago, Chicago, IL 60637, USA

³ Kavli Institute for Cosmological Physics, University of Chicago, Chicago, IL 60637, USA

⁴ Lawrence Livermore National Laboratory, 7000 East Ave., Livermore, CA 94550-9234, USA

⁵ Stockholm University, Universitetsvägen 10, 114 18 Stockholm, Sweden

⁶ SLAC National Accelerator Laboratory, 2575 Sand Hill Road, Menlo Park, CA, 94025, USA

⁷ Kavli Institute for Particle Astrophysics and Cosmology, Stanford University, Stanford CA 94305, USA

⁸ Laboratoire Univers et Particules de Montpellier, Place Eugène Bataillon - CC 72, F-34095 Montpellier Cedex 05, France

⁹ Centre de Physique des Particules de Marseille, 163, avenue de Luminy Case 902 13288 Marseille cedex 09, France

¹⁰ LPC, IN2P3/CNRS, Université Clermont Auvergne, F-63000 Clermont-Ferrand, France

¹¹ HEP Division, Argonne National Laboratory, 9700 S Cass Ave, Lemont, IL 60439, USA

¹² University of Toronto, 27 King's College Cir, Toronto, ON M5S, Canada

¹³ Department of Physics and Astronomy, Rutgers University, Piscataway, NJ 08854, USA

¹⁴ Department of Physics and Astronomy, University of Pittsburgh, 4200 Fifth Ave, Pittsburgh, PA 15260, USA

¹⁵ Pittsburgh Particle Physics, Astrophysics, and Cosmology Center (PITT PACC).

¹⁶ Department of Astronomy, University of Illinois at Urbana-Champaign, Urbana, IL 61801, USA

¹⁷ Center for AstroPhysical Surveys (CAPS), National Center for Supercomputing Applications (NCSA), University of Illinois at Urbana-Champaign, Urbana IL 61801, USA

¹⁸ School of Physics and Astronomy, University of Southampton, University Rd, Southampton SO17 1BJ, United Kingdom.

Received - ; accepted -

ABSTRACT

The Vera Rubin Observatory Legacy Survey of Space and Time (LSST) is expected to process $\sim 10^6$ transient detections per night. To use these transients for precision measurements of cosmological parameters and rates studies, it is critical to understand the detection efficiency, magnitude limits, artifact contamination levels, and biases in the selection and photometry. Here we rigorously test the LSST Difference Image Analysis (DIA) pipeline using simulated images from the Rubin Observatory LSST Dark Energy Science Collaboration (DESC) Data Challenge (DC2) simulation for the Wide-Fast-Deep (WFD) survey area. DC2 is the first large-scale (300 deg^2) image simulation of a transient survey that includes realistic cadence, variable observing conditions, and CCD image artifacts. We analyze $\sim 15 \text{ deg}^2$ of DC2 over a 5-year time-span in which artificial point-sources from Type Ia Supernovae (SNIa) light curves have been overlaid onto the images. We measure the detection efficiency as a function of Signal-to-Noise Ratio (SNR) and find a 50% efficiency at $\text{SNR} = 5.8$ averaged over all bands. The corresponding magnitude limits for each filter are: $u = 23.66$, $g = 24.69$, $r = 24.06$, $i = 23.45$, $z = 22.54$, $y = 21.62$ mag. The artifact contamination levels is $\sim 90\%$ of all detections, corresponding to ~ 1000 artifacts/ deg^2 g band, and falling to $300/\text{deg}^2$ y band. The recovered photometry has biases $< 1\%$ for magnitudes $19.5 < m < 23$. We show that our DIA performance on simulated images is similar to that of the Dark Energy Survey difference-imaging pipeline applied to real images. We also characterize DC2 image properties to produce catalog-level simulations needed for distance bias corrections. We find good agreement between DC2 data and simulations for distributions of SNR, redshift, and fitted light-curve properties. Applying a realistic SNIa-cosmology analysis for redshifts $z < 1$, we recover the input cosmology parameters to within statistical uncertainties. Finally, we discuss further applications of this dataset and analysis, and we suggest pipeline improvements before LSST operations begins.

Key words. image processing – cosmology – Supernovae

1. Introduction

The Vera C. Rubin Observatory Legacy Survey of Space and Time (LSST¹, Ivezić et al. 2019) is expected to soon begin operations and acquire images over 10 years. This survey will use

the Simonyi Survey Telescope at Rubin Observatory, which is a 8.4m class² telescope with a 3.2 Gigapixel camera, yielding a 9.6 deg^2 field of view. The Rubin Observatory LSST Camera design includes *ugrizy* filters, and the expected 5σ r band depth is > 24 (AB system) in a single 30 second visit, where each visit is

¹ <http://www.lsst.org>

² 6.7m of effective collecting area

comprised of two 15 second exposures. The instrument and the survey strategy have been optimized towards obtaining repeated observation of $\sim 20,000 \text{ deg}^2$ of the sky over 10 years.

LSST will explore a broad range of research fields in astrophysics (LSST Science Collaboration et al. 2009); the main science objectives are the study of solar system dynamics, mapping the Milky Way structure, and probing dark matter and dark energy. Many of these science goals rely on the discovery of transient sources, and the expected number of transient detections from all astrophysical variability sources is $\sim 10^6$ per night³ (Ivezić et al. 2019; Ridgway et al. 2014; Graham et al. 2020), an unprecedented rate when comparing to precursor surveys. Past transient surveys have either focused on low redshift ($z < 0.1$) using shallow/wide area strategies, or higher redshift using deep/limited area strategies (see Scolnic et al. 2018 for a review). The unique capabilities of LSST enable survey strategies using wide areas with deep images. To discover transients and measure their light curves, the LSST Project has developed Difference Image Analysis (DIA) software components. The Rubin Observatory LSST Dark Energy Science Collaboration (DESC⁴) used these components to develop an orchestration software layer called `dia_pipe`⁵. In this paper, we make the first evaluation of this pipeline by analyzing simulated images.

Type Ia supernovae (SNIa) are transient events that are used as cosmological probes to measure the expansion history of the universe and in particular the dark energy equation of state w (and its cosmic evolution parameterized by w_a ; The LSST Dark Energy Science Collaboration (DESC) 2019, SRM). LSST is expected to increase the SNIa sample size by up to a factor of 100 compared to previous samples (Betoule et al. 2014; Sako et al. 2018; Scolnic et al. 2018; Jones et al. 2019). Furthermore, the survey will yield the discovery of SNIa using a single instrument with redshifts up to $z \sim 1.2$. The requirements on systematic uncertainties from the SNIa-cosmology analysis are detailed in The LSST Dark Energy Science Collaboration et al. (2018); these requirements include photometric precision at the few mmag-level and accurately determined selection biases.

To rigorously test analysis pipelines before the pre-survey commissioning period, DESC has generated a large and comprehensive set of image simulations known as Data Challenge 2 (DC2) (Sánchez et al. 2020; LSST Dark Energy Science Collaboration et al. 2020). Each DC2 image is based on models of the LSST instrument and expected observing conditions at the summit (sky noise and Point Spread Function - PSF), along with realistic catalogs of galaxies and supernovae light-curves. The full DC2 area covers 300 deg^2 of the Wide-Fast-Deep (WFD) survey and includes injected point sources of Type Ia supernovae with an average cadence of 3 days (15 days in each filter). Using a DC2 subset of 15 deg^2 , we have processed the raw CCD pixels with DIA to characterize SNIa transient finding, photometric precision, and selection effects. In addition, we treat DC2 like real data and perform a cosmology analysis that includes light-curve fitting, bias-correcting distances, and fitting for cosmological parameters w and Ω_M . This pixel-to-cosmology test is a critical part of evaluating `dia_pipe` readiness for survey operations.

The layout of this work is the following. In Section 2 we explain the DC2 dataset used and in Section 3 we give details on the analysis and the techniques implemented. Section 4 shows our results on DC2 data processing, and Section 5 lists perfor-

mance metric scores obtained for transient detection as well as cosmology fitting. In Section 6 we discuss our results and compare them to previously reported analysis. The final discussion and conclusions are presented in Section 7.

2. The DC2 Dataset

The Data Challenge 2 (DC2) is a broad DESC effort to create and process simulated LSST images based on modelling galaxies and transients in the universe (LSST Dark Energy Science Collaboration et al. 2020). The simulation is composed of observations spanning a sky area of 300 deg^2 during 5 years of survey operations. The simulated data includes the expected instrumental signatures from the LSST Camera as well as the atmospheric effects in all six optical bands *ugrizy*. DC2 contains stars, galaxies, and astrophysical effects such as clustering, cosmic web/structure formation, and gravitational lensing effects such as cosmic shear. DC2 also includes variable stars, transient variability from SNe Ia⁶, Active Galactic Nuclei (AGN) galaxies, and strong lensed SNe Ia.

DC2 used the state-of-the-art N-body simulation *Outer Rim* (Heitmann et al. 2019). The cosmological parameters used to create *Outer Rim* are consistent with *WMAP-7* (Komatsu et al. 2011). From this gravity-only simulation, the *cosmoDC2mock* catalog (Korytov et al. 2019) is created; it covers 440 deg^2 of sky area up to a redshift of $z = 3$. *CosmoDC2* contains more than 500 properties for each galaxy, including stellar and halo mass, shape, Spectral Energy Density (SED), central black hole parameters, AGN activity, as well as environment related quantities such as the full gravitational shear and convergence maps of the sky, which gives the observed shape of each galaxy.

In this work we use Run 2.2i Wide Fast Deep (WFD) images with an average transient cadence of 3 days between observations. DC2 images were produced with the image simulation software *imSim*⁷ that imprints observing conditions and instrumental signatures using a model of the LSSTCam. The observing conditions, which include sky noise, Point Spread Function (PSF), zeropoint, and dithering are based on the *minion_1016*⁸ observing strategy produced with the operations simulator software *OpSim*⁹. Each object SED is attenuated from a calculation of Galactic dust extinction and atmospheric effects that includes differential chromatic refraction. Effects from the CCD readout electronics are also simulated, including charge repulsion effects and saturation. Each simulated visit illuminates $189 \text{ k} \times 4 \text{ k}$ CCD detectors (3 billion pixels) covering almost 10 deg^2 , with a plate scale of 0.2 arcsec/px .

A summary of the DC2 SNIa properties is shown in Table 1. For SNIa, the rest frame SED is computed with the SALT2 model (Guy et al. 2010; Betoule et al. 2014). Since the original SED model covers only the *g* and *r* bands in the rest-frame, we use a wavelength-extended model (Pierel et al. 2018) that covers all of the LSST bands. For *imSim* to run properly, we include an additional modification that prevents negative UV spectral fluxes. The properties of each SNIa in DC2 are determined by the following SALT2 parameters: redshift (z), time at peak brightness (t_0), stretch (x_1), color (c), and amplitude (x_0). Each redshift is randomly selected from a volumetric rate, $r_V(z) = 2.5 \times 10^{-5} (1+z)^{1.5} \text{ Mpc}^3 \text{ yr}^{-1}$ (Dilday et al. 2008). The t_0 value is randomly selected within the 5 year DC2 time span.

⁶ No other SN types are included

⁷ <https://github.com/LSSTDESC/imSim>

⁸ <http://ls.st/Collection-4604>

⁹ https://github.com/lsst/sims_operations

³ <https://www.lsst.org/scientists/keynumbers>

⁴ <http://lsstdesc.org>

⁵ https://github.com/LSSTDESC/dia_pipe

Table 1: SNIa properties used in DC2 simulations.

DC2 SNIa property	
Light curve model	SALT2 Extended + 0.15 mag offset* (Pierel et al. 2018)
Rate model	$r_V(z) = 2.5 \times 10^{-5} (1+z)^{1.5} \text{Mpc}^3 \text{yr}^{-1}$ (Dilday et al. 2008)
Intrinsic scatter	$\sigma_{\text{int}} = 0.15 \text{ mag}$
Host correlation	None
Stretch population	$\bar{x}_1 = 0.873$, $\sigma_+ = 1.43$, $\sigma_- = 0.359$, Range= $[-3.0, 2.0]$
Color population	$\bar{c} = -0.048$, $\sigma_+ = 0.043$, $\sigma_- = 0.097$, Range= $[\pm 0.3]$
Luminosity parameters	$\alpha = 0.137$, $\beta = 3.21$

* This offset was a mistake in the DC2 generation, and is included in the simulations for bias corrections.

Each SNIa includes an intrinsic scatter drawn from a Gaussian distribution with $\sigma = 0.15 \text{ mag}$; a coherent mag fluctuation is applied at all SNIa phases and wavelengths. The SALT2 parameters x_1 and c were each drawn from an asymmetric Gaussian distribution with parameters shown in Table 1. The amplitude x_0 is computed from the SALT2 parameters and the luminosity distance. The luminosity parameters α and β were set to 0.137 and 3.21 respectively.

Correlations between the SN Ia and host-galaxy properties were not included in the simulations. Supernovae were assigned to a galaxy using an occupation probability proxy of stellar mass. For host galaxies of SNe Ia, the cosmoDC2 stellar mass distribution peaks at $\sim 10^{11} M_{\odot}$, which is $\sim 5 \text{ dex}$ higher than the typical mass of field galaxies (See Fig. 5 in (LSST Dark Energy Science Collaboration et al. 2020)). 10% of SNe Ia are assigned to be ‘hostless’ in order to provide a control sample of isolated transients.

DC2 images are processed by the LSST pipelines, which organize image data in sets of *tracts* and *patches* for operational purposes. Each 2.56 deg^2 tract is a square containing 7×7 patches that share a common World Coordinate System (WCS) projection. This sky map organization is used for image-coaddition grid resampling, database access and image data manipulation, DIA processing, and template creation. Each DC2 patch contains 4100×4100 pixels (roughly the size of a CCD) with a scale of $0.''2$. To avoid missing area due to edge effects, patches overlap with their neighbors by 100 pixels and tracts overlap by 1 arcmin.

In this work, we select a 15 deg^2 area from the DC2 WFD (hereafter called ‘DC2-SNIa’ area) which includes 1967 LSST-cam visit observations and 105,942 CCD images. We select SNe Ia with redshifts $z \leq 1.0$, which includes the full range of cosmologically useful SNe Ia that will be discovered in the WFD (The LSST Dark Energy Science Collaboration et al. 2018). We discard objects $< 65''$ from the edges of the DC2-SNIa area in order to avoid subtraction artifacts from template overlapping issues. DC2-SNIa contains 5884 Type Ia SNe, and Fig. 1 shows distributions of redshift and SALT2 parameters. Fig. 2 shows the DC2-SNIa sky area used in this work, illustrating the tracts and patches used, and the locations of analyzed SNe Ia.

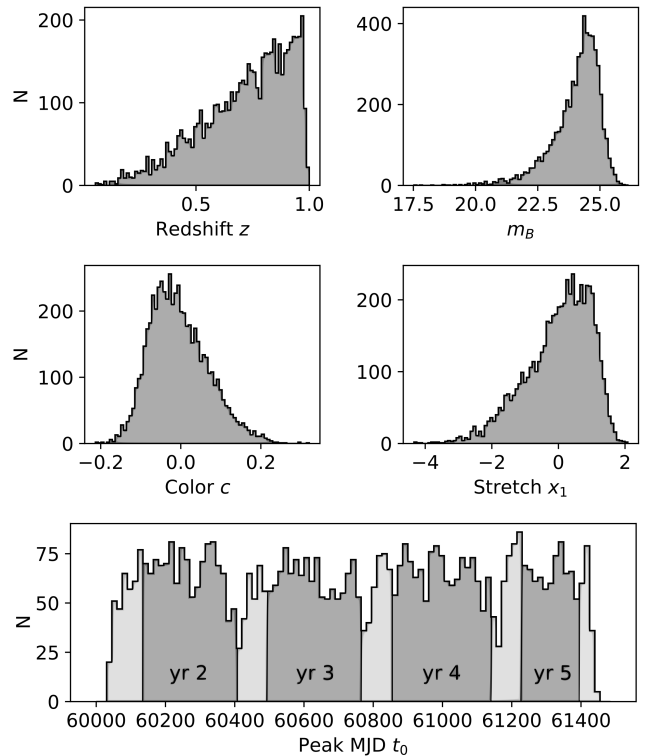


Fig. 1: Distribution of redshift and SALT2 model parameters for DC2 Type Ia Supernovae. The light grey regions (bottom panel) are for events whose peak brightness occurs outside a season of observations.

3. Analysis

Here we describe the *DIA LSST pipeline framework*, and SNIa-cosmological analysis.

3.1. DIA pipeline framework

The Rubin Observatory Data-Management team has developed a state-of-the-art set of software tools for CCD data reduction that contains several routines for image processing, such as image coaddition, flux measurements, etc. This image processing framework, named ‘LSST Science Pipelines’¹⁰, is open source and can be used on any optical and infra-red survey data set. DESC uses the LSST pipelines system to remove instrumental signatures from DC2 images, (e.g., electronic readout bias, dark current, illumination gradients), to calibrate images, and to obtain a World Coordinate System (WCS) solution.

For transient detection, DESC has developed a specific pipeline package *dia_pipe* that uses LSST Science Pipelines’ image processing tools, including Difference Image Analysis (DIA) routines. The central concept of DIA is to compare two images of the same sky area taken at different times, and detect sources that change in brightness. Each image has different properties (such as PSF, sky noise and zeropoint, etc.) and the subtraction accounts for these effects. DIA uses a co-added reference image (*template*) and one recently observed *search image* on which we want to find variability. The reference image is constructed by stacking a subset of archival images taken in exceptional observing conditions with low sky noise, small

¹⁰ <https://pipelines.lsst.io>

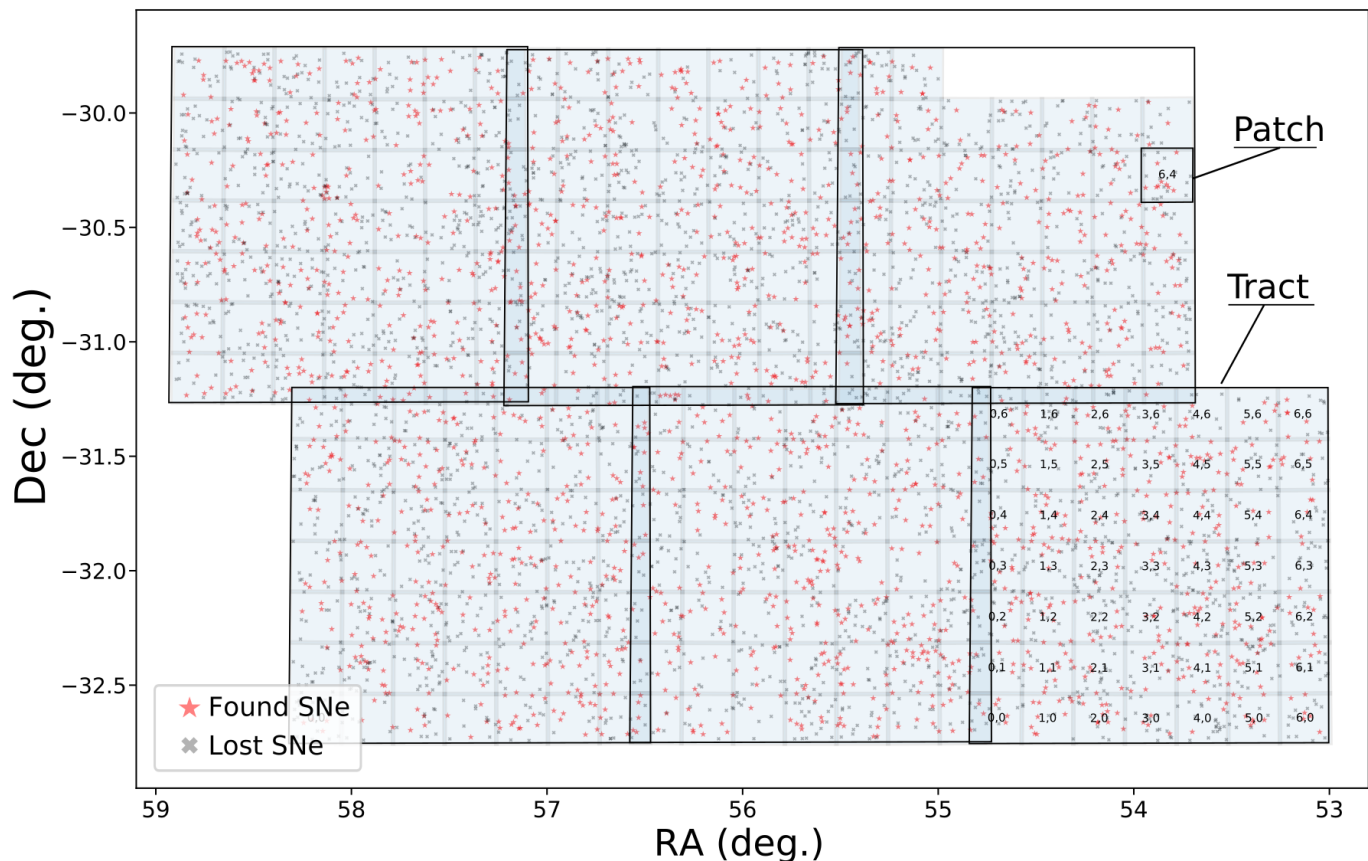


Fig. 2: DC2-SNIa sky area. Small squares indicate patches, and large squares are tracts. Detected and undetected SNe are shown as red stars and grey crosses, respectively. In light-blue we show used patches.

PSF size, and high atmosphere transparency (more details in Sec. 4.1). Since these templates are built from many individual observations, pixels with artifacts (e.g. moving object trails, cosmic rays, CCD blooming and bleeding) are rejected during the co-addition process. In this work, DIA is based on the Alard & Lupton (1998) (hereafter A&L) technique, which uses a kernel to transform the template image such that its pixel locations, orientation, and PSF match the search image.

The `dia_pipe` stages are illustrated in the upper panel of Fig. 3 and briefly described below:

- **Instrumental signature removal and calibration:** Simulated images, including calibration frames (dark current, bias and flat field exposures) are ingested to perform Instrumental Signature Removal (or ISR) and image calibration, resulting in a repository of calibrated image exposures called “*Cal-exp’s*.”
- **Template Coaddition:** From the Calexp repository, 40 images are selected from the first season (Y1) with good seeing and low sky noise. Among these images, those that overlap each DC2 patch by a significant fraction are co-added to build templates. Pixel weight was estimated using the inverse variance.
- **DIA:** The A&L image subtraction algorithm is run on images from seasons 2-5, which produces difference images. Next, source detection is run on each difference image to obtain a catalog of DIA single-visit detections, called `diaSource`. To avoid artifacts near CCD edges, detections within 16 pixels

of an image edge are discarded; this cut is about $\times 3$ larger than the typical PSF-FWHM size. At least one corner of each search image is required to overlap a template image within $65''$ of the edge. The DIA kernel basis is composed of 3 Gaussians, with an adaptive spatially varying size to accommodate varying PSF sizes. The basis components also vary spatially.

- **Association:** a candidate-association algorithm creates `diaObject`s from one or more `diaSource`s that match spatially within $0''.5$. This cut radius is much larger than the average astrometric precision of DC2 calibration (see Fig. 13 of (LSST Dark Energy Science Collaboration et al. 2020)). As each `diaSource` is added to a `diaObject`, the average RA and Dec coordinate of the `diaObject` is updated.
- **Forced photometry:** For each `diaObject`, forced PSF photometry is performed at the location of the object for all overlapping images, regardless of whether there was a `diaSource` detection. The collection of forced photometry fluxes and uncertainties for each `diaObject` comprises the light-curve used in the cosmology analysis (Sec. 3.3).

3.2. DIA validation

Before using the light curves for the cosmology analysis we perform several validation checks on the performance of the DIA steps explained in Sec. 3.1. These validation checks include:

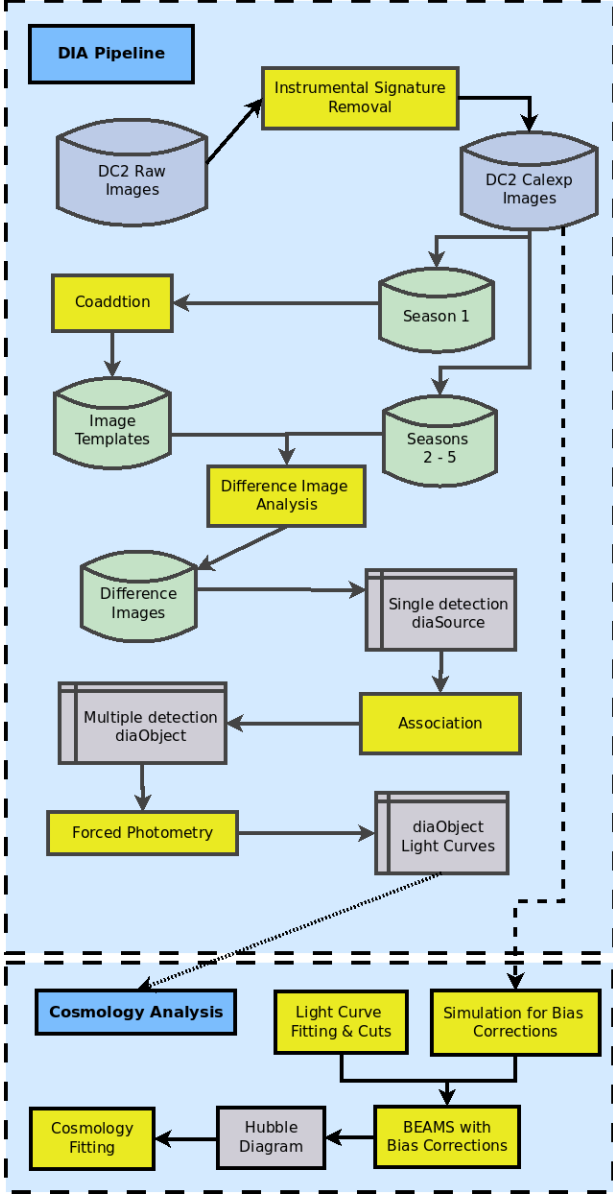


Fig. 3: Diagram of `dia_pipe` and LSST Science Pipelines (upper box). Each processing step (yellow boxes) takes an image (green cylinders) or catalog data (gray tables), and produces new images or catalogs. Additionally we show connections to the cosmology analysis (bottom box).

- Template quality (depth and PSF size)
- Efficiency vs. SNR
- Detection depth per band
- Artifact contamination level
- Photometric precision for fluxes
- Photometric uncertainty correlation with Surface Brightness
- Photometric flux-outlier fractions

3.3. Cosmology analysis

Here we describe a cosmology analysis that combines the DC2 light-curves, obtained with the DIA pipeline framework, with a simulated low redshift (SimLow- z) sample generated with the SNANA simulation. The SimLow- z sample covers a redshift range of $z < 0.08$ with an assumed spectroscopic-selection efficiency of 100%. The “DC2+SimLow- z ” analysis includes light curve fitting to standardize the SNIa brightness, a Monte Carlo simulation to correct for selection effects, a global fit to produce a bias-corrected Hubble diagram, and a w CDM fit to estimate w and Ω_M (see bottom panel in Fig. 3). We closely follow the procedures used in the analyses for Pantheon (Scolnic et al. 2018), PS1 (Rest et al. 2014; Jones et al. 2018), and DES (Brout et al. 2019).

To the extent possible, we treat DC2 light curve data as real data by not using underlying truth information. However, there are four caveats where truth information is used. (1) We do not use DC2 data to train the SALT2 model, nor to measure the true color and stretch populations; instead, we use the known SALT2 model for light curve fitting, and we use the known SALT2 and population model for the bias-correction simulations. (2) We select light curves from `diaObjects` that match true DC2 SNe Ia, and thus our DC2 sample corresponds to a spectroscopically confirmed sample without contamination from other SNe types. (3) We use the true DC2 redshifts, and thus assume accurate redshifts from either the SN or correctly-matched host-galaxy. (4) To characterize DIA detection efficiency vs. Signal-to-Noise Ratio (SNR) we use the same DC2 light curve data as in the analysis; for future LSST analysis of real data, there will be a separate data stream of fake sources to measure this DIA property.

The analysis stages described below use programs from the Supernova Analysis (SNANA: Kessler et al. 2009) software package¹¹:

- **Light curve fitting on data:** we use the SALT2-Extended (Pierel et al. 2018) light curve model, the same model used to generate DC2 SNIa, and fit for t_0 , x_0 , x_1 and c parameters and their covariances. We impose the following selection requirements (cuts) based on previous cosmology analyses:
 - at least one detection (Sec. 5.1) in any passband
 - maximum SNR > 4 in at least 3 separate passbands
 - fitted $|x_1| < 3$, and $0 < \sigma_{x_1} < 2$
 - fitted $|c| < 0.3$
 - fitted peak MJD uncertainty < 3 days
 - fit probability (P_{fit}), computed from χ^2 and the number of degrees of freedom (NDOF), satisfies $P_{\text{fit}} > 0.05$.
 - At least one observation before t_0 , and another 10 days after t_0 in the rest frame.
 - require valid bias correction in BBC (see Hubble Diagram determination below)
- **Simulation for bias corrections:** to prepare for distance bias corrections, we generate a catalog level simulation as described in Kessler et al. (2019). We use DC2 DIA data to determine a cadence library (Section 6.1 of Kessler et al. 2019), detection efficiency vs SNR for each band, and flux

¹¹ <https://github.com/RickKessler/SNANA>

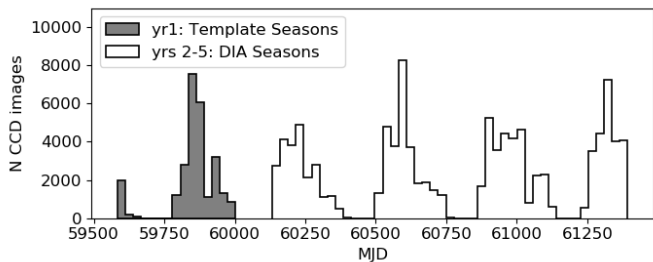


Fig. 4: Distribution of observation dates (MJD) from DC2 images spanning 5 seasons. The first season (shaded) is used for templates.

uncertainty corrections. The same cadence library and detection efficiency were used to simulate both the DC2 and the SimLow-z samples.

- **Hubble Diagram:** we use “BEAMS with Bias Corrections” (Kessler & Scolnic 2017, BBC) to determine a bias corrected Hubble diagram in 9 redshift bins, and to determine nuisance parameters: stretch-luminosity correlation α , color-luminosity correlation β , and intrinsic scatter σ_{int} .
- **Cosmology fitting:** we fit for w and Ω_M using a fast minimization program that combines the DC2+SimLow-z SN Ia Hubble diagram with a cosmic microwave background (CMB) prior using the $R(z_*)$ shift parameter (e.g., see Eq. 69 in Komatsu et al. 2009). To avoid bias from a measured prior, $R(z_*)$ is computed from the DC2 cosmology parameters. To have CMB constraining power similar to that of Planck (Ade et al. 2016), we tuned the uncertainty $\sigma_R = 0.007$ as follows. We use the publicly available DES 3-year SN Ia Hubble diagram,¹² which resulted in $\sigma_w(\text{stat}) = 0.042$ when combined with Planck constraints. We run our fast cosmology fitting program on this DES 3-year sample, and tune σ_R to achieve the same $\sigma_w(\text{stat})$.

4. Data processing results

We processed DC2 image data using six tracts, which comprises a sky area of 15 deg^2 square degrees during 5 observing year-seasons. We used the first year for template creation (Fig. 4) and the remaining 4 years (hereafter called DIA seasons) for image subtractions, creating a total of $\sim 106\text{k}$ DIA images in all LSST filters *ugrizy*.

4.1. Template creation

We show the distributions of the number of images used per template in Fig. 5 in a boxplot format. The distributions peak near 40, and they all have a tail extending down to ~ 15 images due to insufficient overlap with the corresponding patch area.

For the template and DIA season images, photometric properties of PSF and 5σ limiting magnitude depth ($m_{5\sigma}$) are listed in Table 2. We compare $m_{5\sigma}$ for templates and DIA seasons in Fig. 6. The template depth is ~ 1 mag deeper than DIA season images. Fig. 7 shows that the PSF distribution for templates is generally smaller and narrower compared to DIA season visits. The exception is *u*-band, where the template PSF is larger than

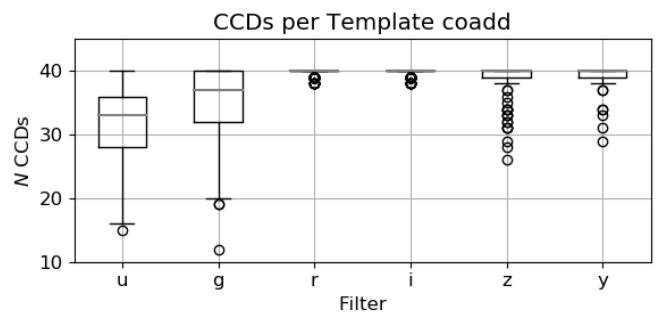


Fig. 5: Distribution boxplots of the number of CCD sensors used per template image (one template per patch, of roughly 14 arc minutes a side). Boxes and whiskers represent 1σ and 3σ width of distribution, with center line indicating the mean value. Outliers are marked with open circles.

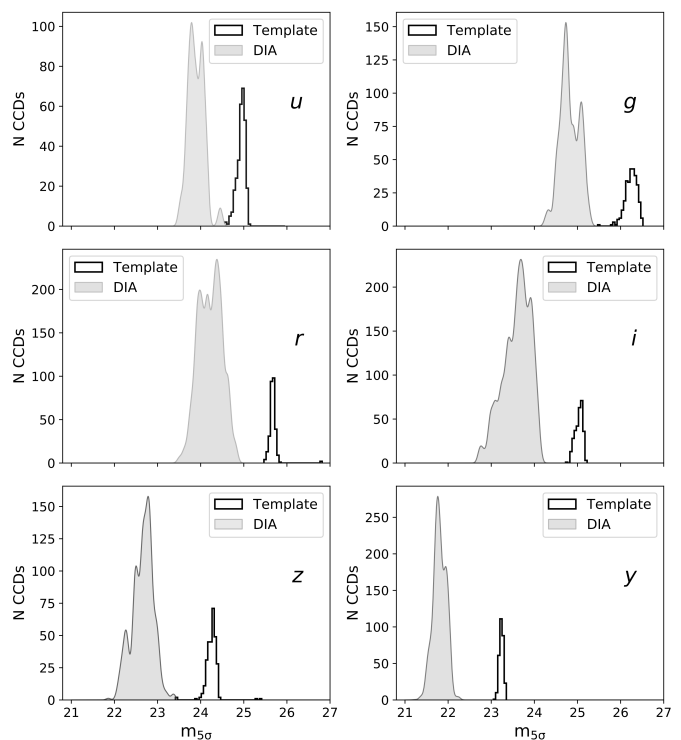


Fig. 6: The $m_{5\sigma}$ distribution for templates, and for visits corresponding to DIA seasons.

for DIA season visits because weather fluctuations caused the first season PSF distribution to be larger than the other seasons.

4.2. Image differences

Our final DIA sample contains a total number of 1967 visits, or 105,942 individual images. In Fig. 8, we show an example of the DIA process from DC2.

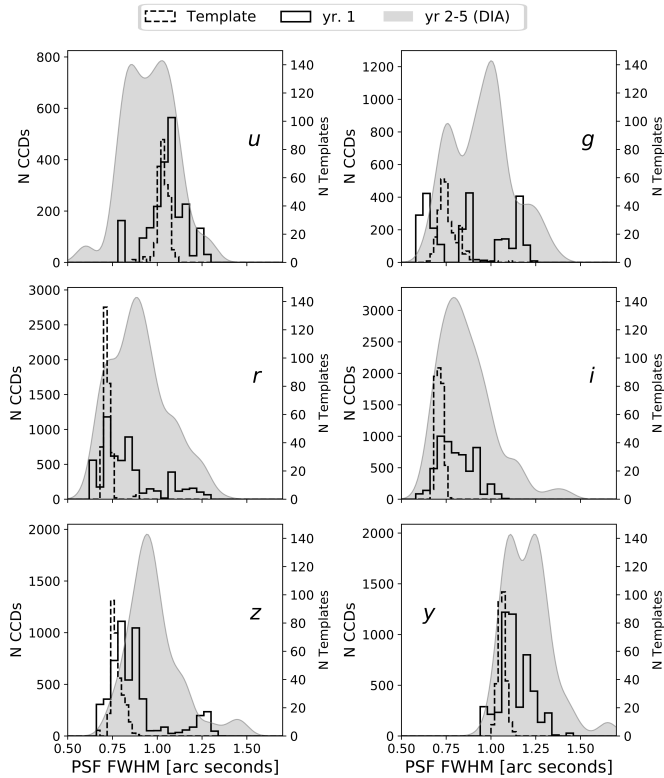
5. Performance metric results

Here we characterize the performance of DIA detections, matching, photometric precision, and level of non-astrophysical detections (subtraction artifacts). For the cosmology analysis, we define metrics based on data-sim distribution overlays of properties

¹² <https://des.ncsa.illinois.edu/releases/sn>

Set	Property	Statistic	u	g	r	i	z	y
Template	$m_{5\sigma}$	mean	24.94	26.24	25.69	25.03	24.25	23.23
		RMS	0.11	0.14	0.16	0.09	0.14	0.05
	PSF [FWHM, arcsec.]	mean	1.03	0.76	0.72	0.71	0.78	1.06
		RMS	0.03	0.06	0.03	0.02	0.03	0.02
DIA seasons	$m_{5\sigma}$	mean	23.89	24.82	24.22	23.59	22.66	21.80
		RMS	0.18	0.22	0.27	0.31	0.25	0.15
	PSF [FWHM, arcsec.]	mean	0.96	0.95	0.90	0.87	0.98	1.21
		RMS	0.14	0.17	0.16	0.15	0.15	0.13

Table 2: Mean and RMS for properties of images used for template co-addition and for DIA season images.


 Fig. 7: PSF size distribution for template coadds (dashed histogram), year 1 (histogram) and DIA season visits (years 2-5, smooth shaded curve), for each LSST filter. Right y-axis correspond to template distribution. For *grizy*, the average template seeing is smaller than for the DIA seasons; for *u* band the average template seeing is larger.

of the light-curves, z -dependent Hubble diagram bias, and fitted cosmology parameters.

5.1. DIA on single detections: *diaSources*

We crossmatch to the truth catalog in two independent steps. First we use the *diaSource* catalog as a reference, and find the closest true SN location on the image. Next we use the true SN catalog as the reference, and find the closest *diaSource*. Finally, we compare these two sets of matches and define a True Positive Match (TP) if there is mutual agreement in both matches, and their separation is below $0''.5$. If a true SN Ia doesn't match a *diaSource* we flag it as a False Negative (FN).

Property	u	g	r	i	z	y
$\text{SNR}_{1/2}$	5.76	5.57	5.87	5.84	5.59	5.60
$m_{1/2}$	23.66	24.69	24.06	23.45	22.54	21.62

 Table 3: Measured $\text{SNR}_{1/2}$ and $m_{1/2}$ vs. filter.

From this procedure, we find a total of 17,719 matches, spanning a wide range of SNR and true magnitudes in all six filters. For the bias-correction simulation, we measure the detection efficiency ($\epsilon = \text{TP}/(\text{TP} + \text{FN})$) as a function of SNR, and characterize this efficiency distribution with $\text{SNR}_{1/2}$ defined as $\epsilon(\text{SNR}_{1/2}) = 0.5$. To better connect the measured ϵ to simulations, we don't use measured SNR, but instead we compute SNR from the true flux and the true noise, where the latter is computed from the zero point, PSF and sky noise (see Eq 11 in Kessler et al. (2019)).

We estimate the value for $\text{SNR}_{1/2}$ by fitting a *sigmoid* function, $\epsilon = (1 + e^{-\text{SNR}})^{-1}$. Fig. 9 shows $\epsilon(\text{SNR})$ for all filters combined; ϵ increases with SNR as expected, and the filter-averaged $\text{SNR}_{1/2} = 5.82$. We also estimate ϵ as a function of magnitude for each bandpass as shown in Fig. 10, which shows a clear correlation with 5σ limiting magnitudes (see Fig.6). For each LSST filter, $\text{SNR}_{1/2}$ and $m_{1/2}$ are listed in Table 3. The $\text{SNR}_{1/2}$ values are between 5.5 and 6 in each band. The $m_{1/2}$ values range from 21.6 in *y* band to > 24 in the *g* and *r* bands.

5.2. Artifact contamination level

To quantify the number of detected artifacts from DIA, we first match *diaSource* detections to all transients in the DC2 truth catalog, using a tolerance of $1''$. We define artifacts as unmatched *diaSources*. Using two bins in PSF seeing size for each filter, Table 4 shows the number of *diaSource* detections, number of matches, and number of artifacts. We show the number of matches for all true astrophysical variables ($N_{\text{diaSrc}}^{\text{var}}$) and true SNe Ia ($N_{\text{diaSrc}}^{\text{SN}}$), along with the percentage of the total number of *diaSource* detections. We characterize artifacts by computing the mean and RMS of the density per square degree (D_{art}). D_{art} is larger for images with smaller PSF, and may in part be due to increased depth for smaller PSF. This effect is most pronounced in *u* band: $D_{\text{art}} \sim 2000$ for $\text{PSF} > 1''$, and increases to ~ 4000 for $\text{PSF} < 1''$. In *g* band, $D_{\text{art}} \sim 1000$ with a 20% difference between the PSF bins. D_{art} falls with increasing wavelength, and is correlated with search depth; in *y* band, $D_{\text{art}} \sim 300$ and the PSF difference is $< 10\%$. From Table 4, $\sim 90\%$ of the *diaSource* detections are artifacts in the *grizy* bands; in *u* band the artifact fraction is 99% due to template seeing size, which is relatively broader than search image PSF size. In previous sur-

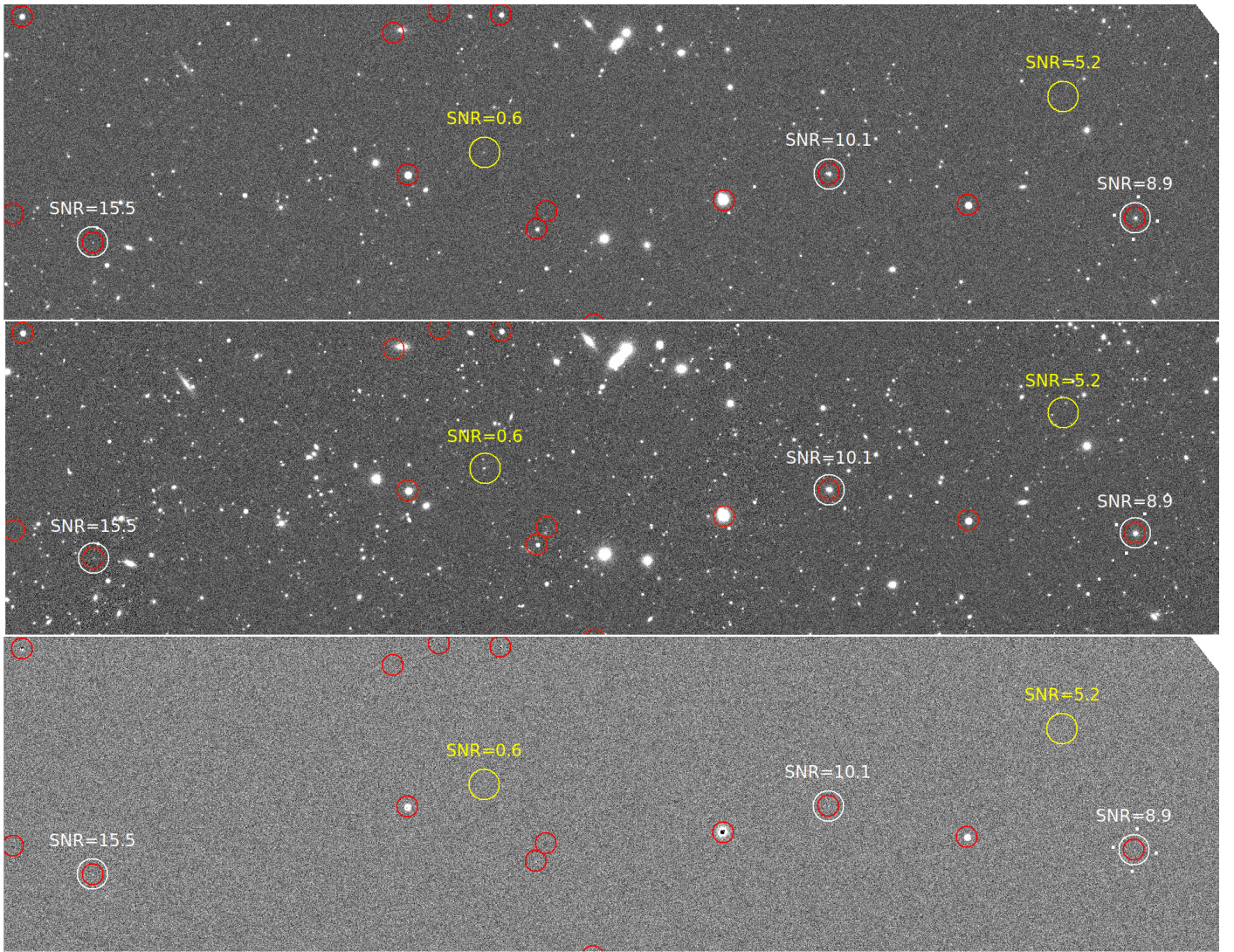


Fig. 8: Example DIA *calexp* image (top), template image (middle), and difference image (bottom) from *dia_pipe*. Red circles show *diaSource* detections, white circles show found transients and yellow circles show missed transients. On top of the circles we include the SNR value of each true transient point source.

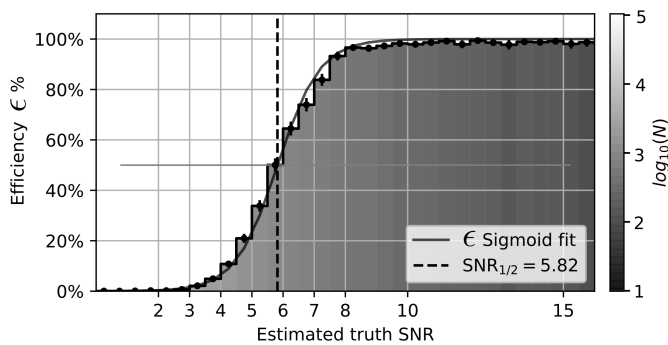


Fig. 9: Detection efficiency (ϵ) vs. calculated SNR. The color scale shows the number of objects per bin, and the dashed vertical line shows $\text{SNR}_{1/2}$.

veys, machine learning methods have significantly reduced artifacts (Goldstein et al. 2015; Kessler et al. 2015; Mahabal et al. 2019), and similar methods are under development within LSST.

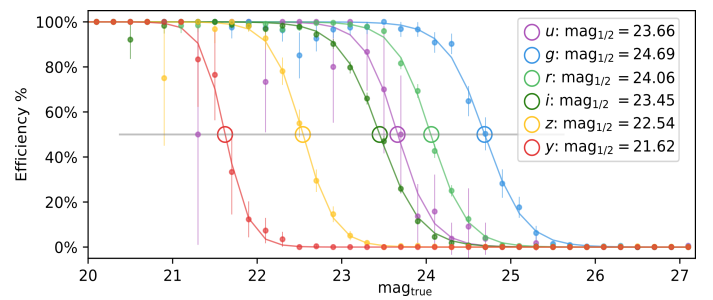


Fig. 10: Detection efficiency vs. true magnitude for each bandpass. Open circles indicate $m_{1/2}$.

5.3. DIA on multiple detections: *diaObjects*

We cross-match the *diaObject* catalog with the true DC2 SNe Ia using a two step procedure (as explained in Sec. 5.1) with a tolerance radius of $0''.5$, finding a total of 2186 matched SNe. Fig. 2 shows the DC2-SN Ia area, and true SNe that were matched and not matched to a *diaObject*. We define SN

Table 4: Number of diaSources detections for SN and artifacts, split into two PSF bins

Filter	N_{CCD}^*	PSF	$\overline{\text{PSF}}$	N_{diaSrc}^+	$N_{\text{diaSrc}}^{\text{SN}^{**}}$	$N_{\text{diaSrc}}^{\text{var}\dagger}$	$N_{\text{diaSrc}}^{\text{art}\ddagger}$	$\overline{D}_{\text{art}}$	$\sigma_{D_{\text{art}}}$
		[arcsec]						[deg ⁻²]	
<i>u</i>	3901	>1.0	1.1	1384171	61 (< 0.01%)	6298 (0.5%)	1377812 (99.5%)	2190	3092
	3902	<1.0	0.9	2999820	71 (< 0.01%)	7815 (0.3%)	2991934 (99.7%)	4189	6620
<i>g</i>	5870	>1.0	1.1	411704	692 (0.17%)	41423 (10.1%)	369589 (89.8%)	956	372
	5870	<1.0	0.8	502003	922 (0.18%)	53411 (10.6%)	447670 (89.2%)	1207	453
<i>r</i>	13905	>0.9	1.0	743402	3146 (0.42%)	76986 (10.4%)	663276 (89.2%)	725	244
	13852	<0.9	0.8	823973	3679 (0.45%)	90830 (11.0%)	729464 (88.5%)	841	288
<i>i</i>	14346	>0.8	1.0	652462	2695 (0.41%)	70934 (10.9%)	578835 (88.7%)	614	227
	13495	<0.8	0.7	724098	3472 (0.48%)	76858 (10.6%)	643768 (88.9%)	736	250
<i>z</i>	7375	>1.0	1.0	279164	361 (0.13%)	30040 (10.8%)	248764 (89.1%)	497	189
	6579	<1.0	0.9	292950	491 (0.17%)	31543 (10.8%)	260916 (89.1%)	591	227
<i>y</i>	8533	>1.2	1.3	177009	66 (0.04%)	20275 (11.5%)	156668 (88.5%)	293	115
	8105	<1.2	1.1	177733	68 (0.04%)	22226 (12.5%)	155439 (87.5%)	312	122

* Number of CCD images

** Number of diaSource detections

+ Number of diaSources matching with SNe (and percentage relative to diaSources)

† Number of diaSources matching with other variable sources (and percentage relative to diaSources)

‡ Number of artifacts (and percentage relative to diaSources)

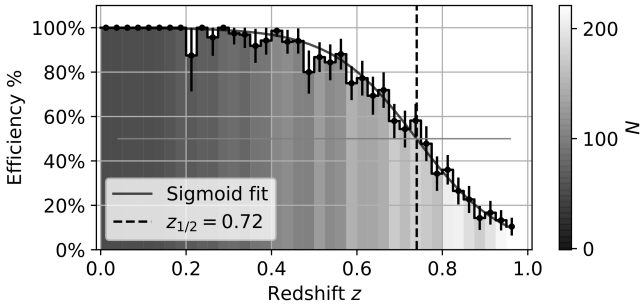


Fig. 11: ϵ_{SN} vs redshift. The dashed vertical line shows where $\epsilon_{\text{SN}} = 0.5$. Gray color scale reflects the number of events per bin.

tection efficiency (ϵ_{SN}) as the probability of associating a true SNIa with a diaObject. Fig. 11 shows ϵ_{SN} vs. redshift for a subsample of true SNe Ia which have been observed more than 5 times, have at least one observation before t_0 , and have at least one observation after $t_0 + 10$ days in the rest-frame. Fitting this distribution to a sigmoid model (as in Sec. 5.1), $\epsilon_{\text{SN}} = 0.5$ at $z = 0.72$.

5.4. DIA photometry: flux measurements

Forced PSF photometry is measured at the diaObject location on all DIA images. Using the set of diaObjects matched with DC2 SNe, we measure flux and magnitude residuals. Fig. 12 shows the fractional photometric bias as a function of true SN magnitude (m_{true}), and the RMS in each bin is illustrated by the $\pm 1\sigma$ envelope. The shaded region shows low-statistics bins with 20 observations, but only 7 events. While there is a hint of bias for bright events, note that correlated residuals among observations from the same event would result in underestimated uncertainties. We accurately measure fluxes for $19 < m_{\text{true}} < 23.25$, where the mean fractional photometric bias values are $< 1\%$. For

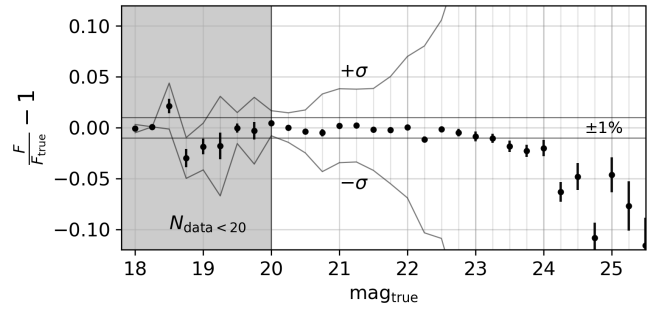


Fig. 12: Mean fractional photometric bias, $F/F_{\text{true}} - 1$, as a function of true SN magnitude. Error bars show uncertainty on the mean, and solid gray lines show the standard deviation ($\pm 1\sigma$) in each bin, as well as the $\pm 1\%$ margin. The shaded area shows bins with less than 20 epochs per bin (a total of 75 observations); these epochs are all from 7 SNe.

magnitudes $m_{\text{true}} > 23.25$ the photometry is biased towards faint values, suggesting a slight bias in the sky subtraction.

5.5. DIA photometry: flux uncertainties

To evaluate the flux uncertainties, we measure the pull distribution in each band (Fig. 13), $(F - F_{\text{true}})/\sigma_F$, where F is the forced photometry flux, σ_F is the uncertainty, and F_{true} is the true flux. Defining

$$\text{RMS}_{\text{pull}} \equiv \text{RMS}[(F_{\text{true}} - F)/\sigma_F], \quad (1)$$

we expect $\text{RMS}_{\text{pull}} = 1$ if the uncertainties are accurate. We find that the distributions are nearly Gaussian, but $\text{RMS}_{\text{pull}} > 1$. For *u*-band $\text{RMS}_{\text{pull}} \sim 1.5$, indicating a significant underestimate of the flux uncertainties. For the other bands, $\text{RMS}_{\text{pull}} \sim 1.1$.

For DES, Kessler et al. (2015) reported a ‘‘Surface Brightness (SB) anomaly’’ in which the true scatter was larger than the reported uncertainties, and this effect was strongly correlated with

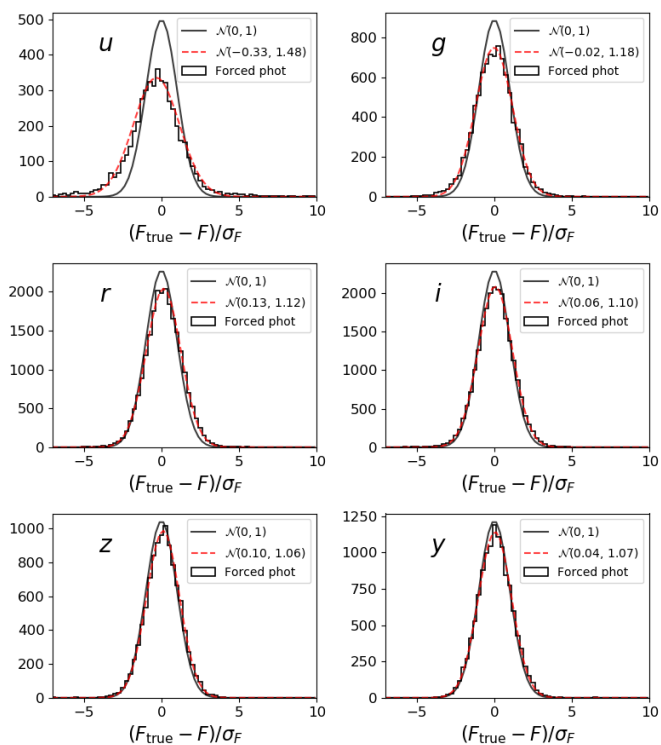


Fig. 13: Distribution of Forced photometry pull values as described in the text. Red curve shows best fit Gaussian model, and black curve is a zero-mean unit-dispersion Normal distribution for comparison.

Table 5: Flux pull distribution parameters

Filter	N	\bar{x}^a	RMS _{pull}	$f_{5\sigma}$ (%) ^b	$f_{10\sigma}$ (%) ^c
<i>u</i>	3936	-0.35	1.48	4.9	2.0
<i>g</i>	8480	-0.03	1.18	0.24	0.09
<i>r</i>	22366	0.15	1.12	0.22	0.05
<i>i</i>	22530	0.06	1.10	0.16	0.04
<i>z</i>	10221	0.10	1.06	0.06	0.01
<i>y</i>	11892	0.05	1.07	0.07	0.02

^a Robust mean of the pull

^b Percent of 5σ outliers.

^c Percent of 10σ outliers.

SB at the SN location. Here we repeat this analysis for DC2 and measure the local surface brightness magnitude (m_{SB}) in template coadds at each SN location, using aperture photometry with a radius of $0''.9$. We find that the SB anomaly is present in DC2 simulated images. Fig. 14 shows RMS_{pull} vs m_{SB} for each filter. RMS_{pull} is near 1 for faint SB, and increases with increasing SB for *grizy* bands. For *u* band, RMS_{pull} ~ 1.5 for all m_{SB} . RMS_{pull} reaches a maximum of ~ 3 in the *g* and *r* bands with $m_{SB} \sim 21$ and $m_{SB} \sim 20$ mag respectively. RMS_{pull} values are consistent for SNe of all peak brightness. This effect is not understood and we therefore apply an empirical scale correction (Fig. 14) to the flux uncertainties. Comparisons with DES are presented in Sec.6.

We show in Table 5 the robust mean and RMS_{pull} for each filter flux pull distribution, as well as the percent of 5σ and 10σ outliers. The *u* band outlier fraction ($\sim 1\%$) is roughly an order of magnitude higher than in the other bands. We found *u* band

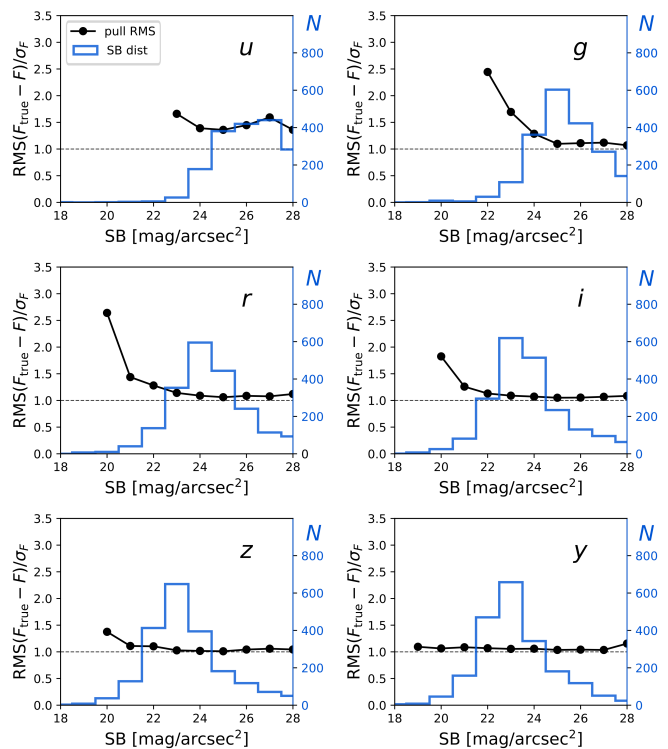


Fig. 14: RMS of forced photometry pull as a function of m_{SB} at the location of each SN. Dashed line shows the unit dispersion reference. The distribution of m_{SB} is also shown for each band.

bias and RMS_{pull} to be anti-correlated with PSF size; the smallest PSF bin has the largest bias and RMS_{pull}.

5.6. Cosmology Analysis Results

Following the steps for cosmology analysis described in Sec 3.3 and shown visually in Fig. 3, we apply the selection requirements and fit light curves with the SALT2 light curve model; a total of 655 events pass cuts (504 for DC2, and 151 for SimLow-z). We also create two catalog-level simulations that have the same DC2/SimLow-z proportion as the data, and undergo the same cuts and light curve fitting as the data: (1) a DATA-like simulation with 2061 events (1560 for DC2 and 501 for SimLow-z) is used to compare data-sim distributions and to crosscheck the analysis, and (2) a large (6.8×10^5 events) bias-correction simulation is used in BBC. The difference between the two simulations is that the latter is generated on a 2×2 grid of α and β to enable interpolating the bias-correction during the BBC fit.

Since the SimLow-z sample is generated by the same catalog simulation used for bias-correction, there is no need to validate this bias-correction. However it is important to validate the bias-correction for DC2 by comparing several distributions between the DC2 data and the DATA-like simulation: the observed magnitude for the brightest flux in each filter (Fig. 15), and SALT2 fit parameters (Fig. 16). All distributions show excellent agreement except for brightest *u*-band mag in Fig. 15.

In Fig. 17 we compare the DC2 detection efficiency vs. redshift, as well as the analysis efficiency vs redshift using the requirements listed in Sec. 3.3. Fitting a sigmoid function to the detection efficiency curves, $z_{1/2} = 0.730 \pm 0.0051$ for DC2 data, and $z_{1/2} = 0.730 \pm 0.003$ for the DATA-like simulation. For

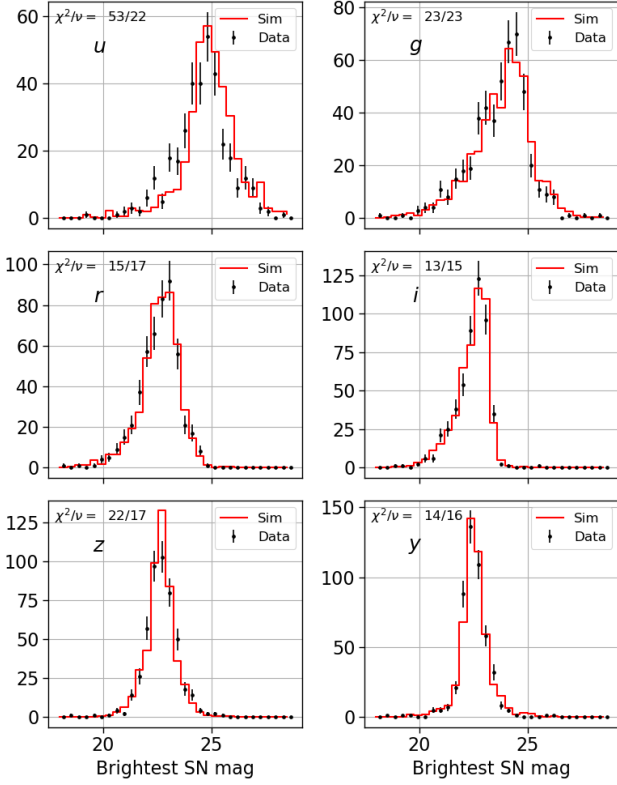


Fig. 15: Distribution of brightest observed mag in each filter for DC2 data (black circles) and DATA-like simulation (red histogram). Each simulated distribution is scaled to match the DC2 sample size. The χ^2 per degrees of freedom (ν) quantifies the data-sim agreement.

the analysis efficiency, $z_{1/2} = 0.58 \pm 0.02$ for DC2 data, and $z_{1/2} = 0.61 \pm 0.01$ for the DATA-like simulation.

The distance bias correction for SimLow- z averages to zero, with small ~ 0.01 mag fluctuations. For DC2, the distance bias correction vs. redshift is shown in Fig. 18 for all events (black circles), where the average bias increases rapidly for $z > 0.6$. The subset of blue ($c < 0.05$) events, which are brighter than average, has a smaller bias in the intermediate redshift range. The fainter subset of red ($c \leq 0.05$) events has a much larger bias at lower redshifts. Accurate simulations and bias corrections are essential for the cosmology analysis.

For the full DC2+SimLow- z sample, Fig. 19 shows the bias corrected Hubble diagram, and the Hubble residuals with respect to the reference DC2 cosmology, for both DC2+SimLow- z data and DATA-like simulation. Using 9 bins of redshift we estimate mean Hubble residuals and error on the mean, shown in the lower panels of Fig. 19; the binned residuals are < 0.04 mag, and consistent with 0, and no clear trend is seen with redshift.

After applying the bias correction analysis to the DATA-like simulation, we measure nuisance and cosmological parameters. Defining the bias on x as $\Delta x \equiv x - x_{\text{true}}$, the biases with respect to input values (Tab. 1) are shown in the “DATA-like Sim” row of Table 6, and these biases are consistent with zero: $\Delta w = -0.002 \pm 0.026$ and $\Delta \Omega_M = 0.001 \pm 0.009$. After this validation, we apply the same treatment to DC2+SimLow- z data and obtain nuisance and cosmological parameters (DC2 row in Table 6). We find $\Delta w = -0.032 \pm 0.046$ and $\Delta \Omega_M = -0.007 \pm 0.013$.

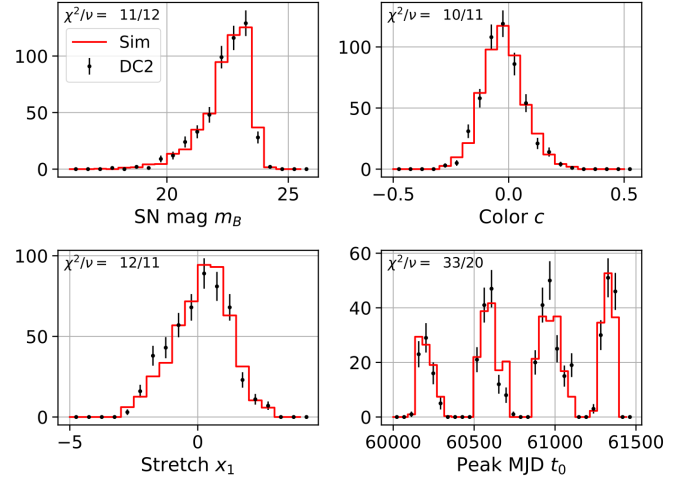


Fig. 16: Distribution of SALT2 fit parameters for DC2 data (black circles) and DATA-like simulation (red histogram). Each simulated distribution is scaled to match the DC2 sample size. The χ^2 per degrees of freedom (ν) quantifies the data-sim agreement.

The nuisance and cosmological parameter biases are consistent with zero.

6. Discussion

Our DIA performance study is similar to that in Kessler et al. (2015) for the Dark Energy Survey (DES), where they used fake light curves injected onto real images during DES operations. In Table 7 we compare several difference-image properties for DC2 and DES. To avoid confusion related to different search depths, we only compare DES bands with similar DC2 depth in Table 3: DES g -band in their deep fields ($m_{1/2} \sim 24.5$ mag) and DES i -band in their shallow fields ($m_{1/2} \sim 23.5$ mag).

For SNR at 50% detection efficiency, the $\text{SNR}_{1/2}$ values are almost identical in g -band, while the DES i -band value is $\sim 10\%$ smaller. To compare the excess scatter on bright galaxies, we evaluate the SB magnitude where the flux-uncertainty scale fac-

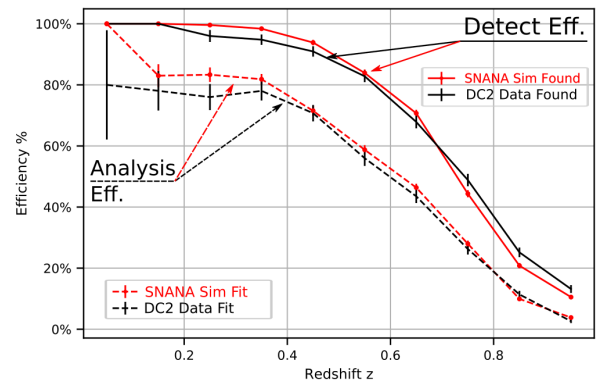


Fig. 17: Detection efficiency vs. redshift in DC2 data (black solid curve), and in DATA-like simulation (red solid). Analysis efficiency vs. redshift for events satisfying cuts and SALT2 fits in DC2 data (black dashed curve) and in DATA-like simulation (red dashed curve).

Table 6: Bias corrected parameter estimation for DC2 sample and simulations.

Data Set	N_{Events}	From Cosmology Fit			From BBC Fit		
		$\Delta w = w - w_{\text{true}}$	$\Delta\Omega_M = \Omega_M - \Omega_M^{\text{true}}$	χ^2/ν	$\Delta\alpha = \alpha - \alpha_{\text{true}}$	$\Delta\beta = \beta - \beta_{\text{true}}$	$\sigma_{\text{int}}/\sigma_{\text{int}}^{\text{true}}$
DC2+SimLow-z	655	-0.032 ± 0.046	-0.007 ± 0.013	11/8	-0.004 ± 0.010	-0.15 ± 0.14	1.02
DATA-like Sim	2061	-0.002 ± 0.026	0.001 ± 0.009	12/8	0.004 ± 0.005	-0.12 ± 0.06	0.94

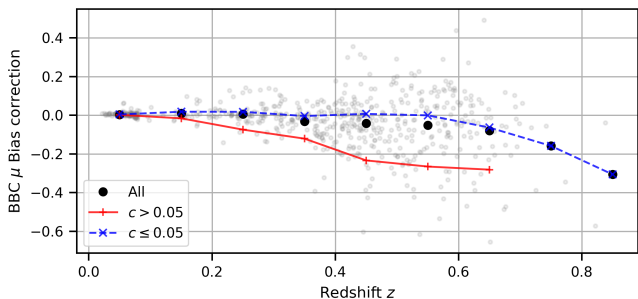


Fig. 18: Average DC2 bias correction vs. redshift for BBC fitted distances. Black dots are for all events, blue curve is for fitted SALT2 color $c < 0.05$, red curve is for $c > 0.05$.

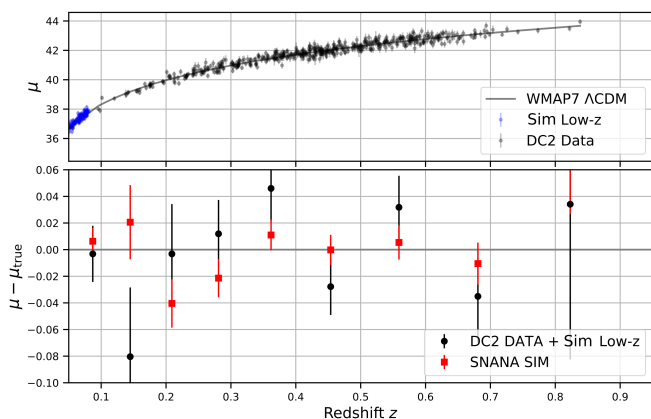


Fig. 19: Bias corrected Hubble Diagram for DC2 data (top) and redshift-binned Hubble residuals for DC2 data and DC2-like simulation (bottom).

tor is 2: $m_{\text{SB}}(\text{RMS}_{\text{pull}}=2)$. These m_{SB} values are nearly identical in g -band (22.1 and 22.0 mag for DC2 and DES, respectively), but differ by 0.7 mag in the i -band (19.8 and 21.5 mag). The $m_{\text{SB}}(\text{RMS}_{\text{pull}}=2)$ values for all DC2 bands are shown in Table 8. The number of detection artifacts per deg^2 is also similar; DC2 is a factor of 2 higher for g -band, and 7% smaller in i -band. Finally, the 5σ flux-outlier fractions for DC2 are about a factor of 2 smaller compared to DES; the corresponding 10σ outlier fractions are much more similar. Assessing the overall performance, DC2 appears to be slightly better because of the improved $m_{\text{SB}}(\text{RMS}_{\text{pull}}=2)$ in the i -band and the reduced 5σ flux-outliers. While this DC2-vs-DES comparison is encouraging for `dia_pipe`, the processing of simulated DC2 images may be giving somewhat optimistic results compared to real data.

The SB anomaly is present in both DES and DC2, but still not understood. Follow-up to DC2 simulations would enable modifying various atmospheric or detector effects to trace the

Table 7: Difference image properties for DC2 and DES.

	DC2- g	DES- g^*	DC2- i	DES- i^{**}
$m_{1/2}$	24.7	24.5	23.5	23.5
$\text{SNR}_{1/2}$	5.57	5.61	5.84	5.36
$m_{\text{SB}}(\text{RMS}_{\text{pull}}=2)$	22.1	22.0	19.8	21.5
$\overline{D}_{\text{art}}$	1080	520	680	730
$f_{5\sigma}(\%)$	0.24	0.49	0.16	0.25
$f_{10\sigma}(\%)$	0.09	0.09	0.04	0.06

* From DES SN Deep fields, to match DC2- g depth.

** From DES SN Shallow fields, to match DC2- i depth.

origin of the anomaly. Improving DIA is important for studies of transients near cores of bright galaxies.

A similar DIA efficiency study was done by the Palomar Transient Factory (PTF, Frohmaier et al. 2017) using ~ 7 million artificial point sources overlaid on PTF images. They characterized their real-time detection efficiency as a function source magnitude, host galaxy surface brightness, and various observing conditions. Their efficiencies are mostly parameterized by surface brightness, and thus cannot be directly compared with our DC2 results using SNR. Nevertheless, they report a $m_{1/2} \simeq 20.3$ in R band for PTF 48 inch class instrument. As shown in DES, PTF, and this DC2 analysis, the detection efficiency has not been analytically modelled and was therefore determined empirically with fake sources.

DIA performance depends critically on using template images with exceptional quality, in particular a narrower PSF with respect to search images. We created templates using Y1 data, and found that poor u -band seeing in Y1 (Fig. 7) degraded DIA for u band, where we find a drop in detection efficiency, as well as biases in photometric flux and uncertainty. The u band filter transmission is much lower than for the other bands, and it is unlikely to discover SNIa because they are faint in the UV; nonetheless, u band is useful for photometric classifiers to distinguish between SNe Ia and core collapse SNe.

The level of artifact detections from DIA is consistent with DES (Table 7). Machine Learning (ML) methodologies are expected to reduce this contamination significantly, according to results obtained by several collaborations (Brink et al. 2013; Goldstein et al. 2015; Mahabal et al. 2019; Duev et al. 2019). We find that the density of artifact detections decreases with increasing PSF size in the search image. This effect might be caused by the DIA kernel transformation, which performs better when the search and template PSF difference becomes larger (Liu et al. *in prep.*).

The DC2 baseline cadence is sub-optimal with respect to the recent developments in LSST cadence studies (Scolnic et al. 2018; Lochner et al. 2018, 2021). Repeating this DC2 image simulation and analysis on alternative cadences is impractical from both a computational and human-effort perspective. To rigorously evaluate alternative cadences, however, this DC2 analy-

Table 8: $m_{SB}(\text{RMS}_{\text{pull}=2})^a$ for each DC2 band.

u_{SB}	g_{SB}	r_{SB}	i_{SB}	z_{SB}	y_{SB}
$-^b$	22.1	20.5	19.8	19 ^c	$-^b$

^a Surface brightness [mag/arcsec²] where flux-uncertainty scale is ~ 2

^b Scale is always < 2

^c Estimated from extrapolation

sis demonstrates that the SNANA simulation can rapidly generate light curve samples that accurately model a full DIA analysis on images. The SNANA simulation uses meta-data from images and DIA that includes cadence, zero point, PSF, sky noise, detection efficiency vs. SNR, and flux-uncertainty vs. SB. A recommended simulation upgrade is to model catastrophic flux-outliers shown in Table 5.

7. Conclusions

In this work, we show results of an integrated Difference Image Analysis pipeline, built using DESC’s `dia_pipe` and LSST pipelines, to analyze simulated images that include SN Ia light curves. Using a light curve catalog compiled from `dia_pipe` results, we applied a commonly used SN Ia standardization method to measure cosmic distances and cosmological parameters. This is the first time that a survey team has carried out such a pixel-to-cosmology test before commissioning operations begin. This analysis is an important stepping stone, enabling monitoring of pipeline performance evolution from survey simulations to real-time analysis during operations.

We have analyzed 15 deg² of DC2 WFD images using LSST DESC’s `dia_pipe` pipeline framework for difference-imaging and transient discovery. The detection efficiency is $\sim 100\%$ for point sources with $\text{SNR} \geq 8$, and is 50% efficient for events with $\text{SNR} \sim 5.8$. Comparing DC2 and DES in bands with the same search depth, the difference-image properties are quite similar (Table 7). To the extent that the simulated DC2 images are realistic, this comparison shows that `dia_pipe` is already performing at the level of a stage III precursor survey that was focused on precision measurements of cosmological parameters.

We apply a cosmology analysis using a SALT2+BBC framework, resulting in 655 SN Ia light curves (504 for DC2, 151 for SimLow-z). To correct for distance biases in BBC, we used SNANA to generate a DATA-like simulation of SN Ia light curves using measured DC2 image properties (PSF, zero point, sky noise) and measured DIA properties (efficiency vs. SNR, flux-uncertainty scale vs. SB). Both the DC2 and DATA-like simulated samples were used to measure w and Ω_M from a bias-corrected Hubble diagram; in both cases we recovered the true cosmological and nuisance parameter values within statistical uncertainties.

We emphasize that the pipeline system is still in active development and may improve by the time LSST starts operations. The pre-commissioning analysis of DC2 is a central contribution for operational readiness.

Acknowledgements.

Author contributions are listed below.

B. Sánchez: Lead design, performed DIA, writing.

R. Kessler: Co-lead project, SNANA simulations and analysis, writing.

D. Scolnic: Lead design and writing.

B. Armstrong: Main `dia_pipe` software developer; draft reviewer.

R. Biswas: DC2 simulation; analysis and data preparation.

J. Bogart: DC2 database storage, access and curation.

J. Chiang: Computing infrastructure, DC2 data access and analysis.

J. Cohen-Tanugi: DC2 image processing and data retrieval.

D. Fouchez: Internal reviewer; suggested paper text and figures edits.

P. Gris: SNWG convener; SNIa discussions.

K. Heitmann: DC2 simulations, paper comments.

R. Hložek: Early discussions, DC2 analysis software.

S. Jha: Internal reviewer; suggested edits to paper text and figures.

H. Kelly: Computing infrastructure; data processing.

S. Liu: DIA analysis tests and debugging.

G. Narayan: DIA analysis discussion, SNIa discussions

B. Racine: DIA analysis discussion; data visualization.

E. Rykoff: DC2 metadata extraction.

M. Sullivan: TD Working Group convener.

C. Walter: DIA discussion and comments.

M. Wood-Vasey: Consulted on several DIA aspects; DESC builder.

B.S and D.S. are supported by DOE grant DE-SC0010007. D.S. is also supported by DOE grant DE-SC0021962 and the David and Lucile Packard Foundation. The DESC acknowledges ongoing support from the Institut National de Physique Nucléaire et de Physique des Particules in France; the Science & Technology Facilities Council in the United Kingdom; and the Department of Energy, the National Science Foundation, and the LSST Corporation in the United States. DESC uses resources of the IN2P3 Computing Center (CC-IN2P3–Lyon/Villeurbanne - France) funded by the Centre National de la Recherche Scientifique; the National Energy Research Scientific Computing Center, a DOE Office of Science User Facility supported by the Office of Science of the U.S. Department of Energy under Contract No. DE-AC02-05CH11231; STFC DiRAC HPC Facilities, funded by UK BIS National E-infrastructure capital grants; and the UK particle physics grid, supported by the GridPP Collaboration. This work was performed in part under DOE Contract DE-AC02-76SF00515.

This work was completed in part with resources provided by the University of Chicago’s Research Computing Center. This work has gone through DESC internal review process, and main authors would like to explicitly thank Saurabh Jha, Dominique Fouchez, and Bob Armstrong for their comments.

This research has made use of the following Python software packages: Astropy (Astropy Collaboration et al. 2013, 2018), Matplotlib (Hunter 2007), Pandas (McKinney et al. 2010), NumPy (van der Walt et al. 2011), Seaborn (Waskom et al. 2014), SciPy (Virtanen et al. 2020).

References

- Ade, P. A., Aghanim, N., Arnaud, M., et al. 2016, *Astronomy & Astrophysics*, 594, A13
- Alard, C. & Lupton, R. H. 1998, *ApJ*, 503, 325
- Astropy Collaboration, Price-Whelan, A. M., Sipőcz, B. M., et al. 2018, *AJ*, 156, 123
- Astropy Collaboration, Robitaille, T. P., Tollerud, E. J., et al. 2013, *A&A*, 558, A33
- Betoule, M., Kessler, R., Guy, J., et al. 2014, *A&A*, 568, A22
- Brink, H., Richards, J. W., Poznanski, D., et al. 2013, *MNRAS*, 435, 1047
- Brout, D., Scolnic, D., Kessler, R., et al. 2019, *The Astrophysical Journal*, 874, 150
- Dilday, B., Kessler, R., Frieman, J. A., et al. 2008, *The Astrophysical Journal*, 682, 262
- Duev, D. A., Mahabal, A., Masci, F. J., et al. 2019, *Monthly Notices of the Royal Astronomical Society*, 489, 3582
- Frohmaier, C., Sullivan, M., Nugent, P. E., Goldstein, D. A., & DeRose, J. 2017, *ApJS*, 230, 4
- Goldstein, D. A., D’Andrea, C. B., Fischer, J. A., et al. 2015, *The Astronomical Journal*, 150, 82
- Graham, M. L., Bellm, E., Guy, L., & Slater, C. T. 2020, *LSST Alerts : Key Numbers*

- Guy, J., Sullivan, M., Conley, A., et al. 2010, *Astronomy & Astrophysics*, 523, A7
- Heitmann, K., Finkel, H., Pope, A., et al. 2019, *The outer rim simulation: A path to many-core supercomputers*
- Hunter, J. D. 2007, *Computing in Science and Engineering*, 9, 90
- Ivezić, Ž., Kahn, S. M., Tyson, J. A., et al. 2019, *The Astrophysical Journal*, 873, 111
- Jones, D. O., Scolnic, D. M., Foley, R. J., et al. 2019, *ApJ*, 881, 19
- Jones, D. O., Scolnic, D. M., Riess, A. G., et al. 2018, *ApJ*, 857, 51
- Kessler, R., Brout, D., D’Andrea, C. B., et al. 2019, *Mon. Not. R. Astron. Soc.*, 485, 1171
- Kessler, R., Marriner, J., Childress, M., et al. 2015, *The Astronomical Journal*, 150, 172
- Kessler, R. & Scolnic, D. 2017, *Astrophys. J.*, 836, 56
- Komatsu, E., Dunkley, J., Nolta, M. R., et al. 2009, *ApJS*, 180, 330
- Komatsu, E., Smith, K. M., Dunkley, J., et al. 2011, *ApJS*, 192, 18
- Korytov, D., Hearin, A., Kovacs, E., et al. 2019, *ApJS*, 245, 26
- Lochner, M., Scolnic, D., Almoubayyed, H., et al. 2021, *arXiv e-prints*, arXiv:2104.05676
- Lochner, M., Scolnic, D. M., Awan, H., et al. 2018, *arXiv e-prints*, arXiv:1812.00515
- LSST Dark Energy Science Collaboration, Abolfathi, B., Alonso, D., et al. 2020, *13 KEVIN REIL*, 12, 13
- LSST Science Collaboration, Abell, P. A., Allison, J., et al. 2009, *LSST Science Book, Version 2.0*
- Mahabal, A., Rebbapragada, U., Walters, R., et al. 2019, *Publications of the Astronomical Society of the Pacific*, 131, 038002
- McKinney, W. et al. 2010, in *Proceedings of the 9th Python in Science Conference*, Vol. 445, Austin, TX, 51–56
- Pierel, J. D. R., Rodney, S., Avelino, A., et al. 2018, *PASP*, 130, 114504
- Rest, A., Scolnic, D., Foley, R. J., et al. 2014, *ApJ*, 795, 44
- Ridgway, S. T., Matheson, T., Mighell, K. J., Olsen, K. A., & Howell, S. B. 2014, *Astrophysical Journal*, 796, 53
- Sako, M., Bassett, B., Becker, A. C., et al. 2018, *Publications of the Astronomical Society of the Pacific*, 130, 064002
- Sánchez, F. J., Walter, C. W., Awan, H., et al. 2020, *arXiv e-prints*, arXiv:2001.00941
- Scolnic, D., Kessler, R., Brout, D., et al. 2018, *ApJ*, 852, L3
- Scolnic, D. M., Jones, D. O., Rest, A., et al. 2018, *The Astrophysical Journal*, 859, 101
- Scolnic, D. M., Lochner, M., Gris, P., et al. 2018, *arXiv e-prints*, arXiv:1812.00516
- The LSST Dark Energy Science Collaboration, Mandelbaum, R., Eifler, T., et al. 2018, *arXiv e-prints*, arXiv:1809.01669
- The LSST Dark Energy Science Collaboration (DESC). 2019, *LSST DESC Science Roadmap*
- van der Walt, S., Colbert, S. C., & Varoquaux, G. 2011, *Computing in Science and Engineering*, 13, 22
- Virtanen, P., Gommers, R., Oliphant, T. E., et al. 2020, *Nature Methods*, 17, 261
- Waskom, M., Botvinnik, O., Hobson, P., et al. 2014, *seaborn: v0.5.0* (November 2014)